



The oxidation of iron in amphiboles at high temperatures: a review and implications for large-scale Earth processes

Giancarlo Della Ventura^{1,2,3} · Simone Bernardini¹ · Gunther J. Redhammer⁴ · Federico Galdenzi¹ · Francesco Radica⁵ · Augusto Marcelli^{2,6} · Frank C. Hawthorne⁷ · Roberta Oberti⁸ · Boriانا Mihailova⁹

Received: 22 September 2024 / Accepted: 4 November 2024
© The Author(s), under exclusive licence to Accademia Nazionale dei Lincei 2024

Abstract

In this paper, we review 10 years of research on high-temperature oxidation process on amphiboles with variable composition. One notable feature that has emerged from our experiments is that iron oxidation is reversible over a relatively large thermal range before the kinetic energy of delocalized electrons and H^+ ions becomes high enough to allow their ejection from the crystal. Experiments under different oxidation conditions showed that the sodic amphibole riebeckite follows two distinct paths: under oxidizing conditions, it undergoes both Fe oxidation and dehydrogenation and the resulting oxo-riebeckite is stable up to ~ 900 °C; under vacuum conditions, neither Fe oxidation nor dehydrogenations occur, and the amphibole is stable up to 800 °C, via a rearrangement of the octahedral cations. In situ HT Raman measurements on grunerite provided the first atomic-scale proof for the thermal activation of polarons in Fe-amphiboles; further studies showed that this process is a general feature of Fe^{2+} -bearing amphiboles. For riebeckite, it starts at 227 °C and is complete at 377 °C under both reducing and oxidizing conditions. Above 377 °C, external oxygen triggers the expulsion of H^+ and e^- from the crystal. The temperature range observed for the development of charge carriers accurately fits the temperatures for the development of high-conductivity layers in warm and cold subduction zones and provides the atomic-scale picture for large-scale processes such as the development of anomalous conductivity layers at convergent-plate margins. Our work shows that Raman spectroscopy may provide relatively straightforward access to the properties of rock-forming minerals of geophysical interest.

This paper is part of the Topical Collection "Minerals as treasure trove for scientific discoveries" originated from the international and interdisciplinary meeting held at the Accademia Nazionale dei Lincei in Rome on February 14-15, 2024.

✉ Giancarlo Della Ventura
giancarlo.dellaventura@uniroma3.it

¹ Department Sciences, University of Roma Tre, Rome, Italy

² LNF-INFN, Frascati (Rome), Italy

³ INGV, Via di Vigna Murata 605, 00143 Rome, Italy

⁴ Department Chemistry Physics of Materials, University of Salzburg, Jakob-Haringerstr. 2A, 5020 Salzburg, Austria

⁵ INGEO Department, University of Chieti-Pescara 'G. d'Annunzio', Chieti, Italy

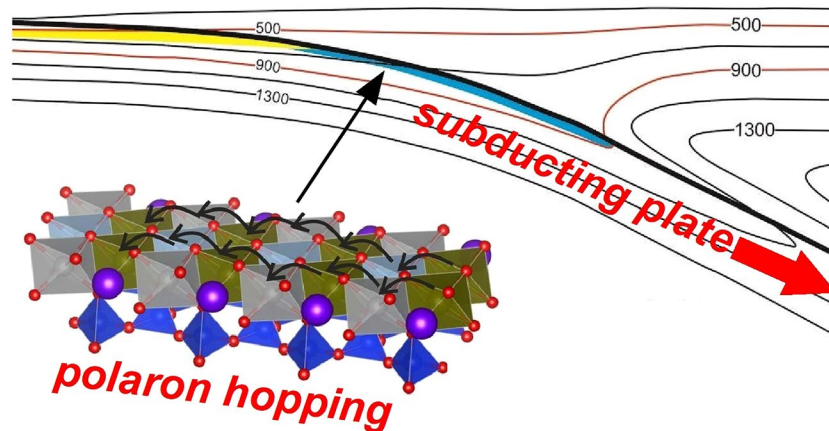
⁶ Rome International Center for Materials Science Superstripes, RICMASS, Rome, Italy

⁷ Department of Earth Sciences, University of Manitoba, Winnipeg, MB R3T 2N2, Canada

⁸ CNR-Istituto di Geoscienze e Georisorse, Pavia, Italy

⁹ Fachbereich Erdsystemwissenschaften, Universität Hamburg, Hamburg, Germany

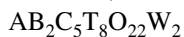
Graphical abstract



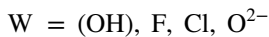
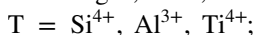
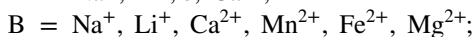
Keywords Fe-amphiboles · HT iron oxidation · Deprotonation · Kinetics · Resonance Raman scattering · Conductivity

1 Introduction

Reactions of hydrous minerals at high temperatures (HT) involve first migration or diffusion and finally loss of hydrogen (*e.g.*, Aines and Rossman 1985; Zang et al. 2005, 2006; Della Ventura et al. 2015a, 2015b). These processes may be associated with simultaneous oxidation of multi-valence elements, typically Fe or Mn, with significant consequences on the physical properties (*i.e.*, electrical conductivity and/or magnetic). Among rock-forming minerals, a notable case is provided by amphiboles, having the general formula (Hawthorne 1983; Hawthorne and Oberti 2007).



Where.



Iron-dominant sodic amphiboles (riebeckite and its asbestos variety crocidolite) were extensively studied at HT during the 1960–1970's (see Addison et al. 1962a, 1962b; Addison and Sharp 1962, 1968; Hodgson et al. 1965; Addison and White 1968; Ernst and Wai 1970 among others) because of their technological applications, the most important of which was insulation from heat and fire. The general features of the dehydrogenation¹ mechanism were sketched during

¹ Note that the terms *dehydration* and *dehydrogenation*, although commonly used as synonyms, have different meanings. Dehydration involves a reaction in which a hydrous phase breaks down with increasing temperature, releases H₂O, and transforms into a new mineral, typically in prograde metamorphic reactions. On the other hand,

these early studies, but the structural adjustments accompanying the oxidation of iron and the loss of hydrogen were not addressed until later (Ungaretti 1980; Phillips et al. 1988, 1989, 1991). Despite these efforts, notable issues such as the dynamics of iron oxidation and the diffusion of electrons and hydrogen ions throughout the mineral during thermal treatment remained unclear. It is worth noting that understanding the oxidation mechanisms of Fe-rich amphiboles has important implications in several fields of science including Geology/Petrology, Geophysics, Materials science, and also Medical Sciences, because it is now clear that the toxic potential of mineral fibers is related to the availability and redox reactions of iron ions at the fiber surface (*e.g.*, Turci et al. 2017; Vigliaturo et al. 2022). Regarding this issue, the recent work of Ballirano and Pacella (2020) shows that Fe-containing tremolite from Maryland (USA) undergoes significant cation rearrangement upon thermal treatment with migration of Fe³⁺ at M(1) and M(3), the most exposed octahedral sites at the amphibole surface; this being the case Fe³⁺ is available for participating to Fenton-type reactivity, thus increasing the mineral toxicity.

Footnote 1 (continued)

dehydrogenation indicates diffusion and loss of H⁺ from the structure without necessarily implying phase decomposition. Dehydrogenation may occur in Fe- and OH-bearing minerals where the Fe²⁺ to Fe³⁺ conversion with increasing temperature is locally balanced by H⁺ loss; in such a case, the mineral may simply transform into its oxo-counterpart basically retaining its atomic arrangement (*e.g.*, Oberti et al. 2018).

2 Amphibole crystal-chemistry: basic concepts

Amphiboles are important silicates and are widespread in different geological occurrences, including igneous, metamorphic, and sedimentary rocks (Deer et al. 1997).

The crystal chemistry of the amphiboles is the most complex of the rock-forming minerals as their structure can incorporate a wide range of ions (see above) in a wide range of coordination numbers. Natural amphiboles crystallize in four possible space groups, although $C2/m$ is by far the most common (Hawthorne and Oberti 2007); a peculiar synthetic amphibole with triclinic symmetry and excess OH has been also described (Cámara et al. 2004). Polyhedra are named according to their central site: e.g., $M(1)$ octahedron, $T(2)$ tetrahedron. The structure (Fig. 1a) can be described as I-beams consisting of ribbons of T -tetrahedra [built by $T(1)$ and $T(2)$ sites] sandwiching ribbons of $M(1)$, $M(2)$, and $M(3)$ octahedra (Fig. 1b) containing C-type cations (Fig. 1c, d); the I-beams are connected via additional [6]- to [8]-coordinated B-cations at the $M(4)$ site (schematically represented as brown spheres in Fig. 1e) that impart significant flexibility to the structure. Notably, the arrangement of T and M polyhedra creates channels of nanometric size ($\sim 1 \times 2$ nm² in section) extending in the c -direction (labelled by A in Fig. 1a); these channels may be empty or occupied by large A-type monovalent cations, commonly Na⁺ and K⁺ but also Ca²⁺ in some rare species (Hawthorne et al. 1996). This atomic arrangement also determines their perfect cleavage and fibrous nature (Gunter et al. 2007). Importantly, OH⁻ groups (more rarely F⁻, Cl⁻ or O²⁻) occur at the O(3)

site coordinating the trimer of $M(1,3)$ octahedra, and is located at the center of a six-membered TO₄-ring (Fig. 1b, c). The presence of hydrogen is one of the most notable features of these silicates; as discussed later, with increasing temperature, H⁺ ions may become mobile, providing a local charge-balance buffering for polyvalent substitutions. The important point here is that this process may enlarge the stability field of the amphiboles, a feature that does not occur in many other common rock-forming silicates such as olivine or pyroxene.

The amphibole structure can accommodate major or minor constituent cations with radii from 0.25 to 1.6 Å and formal charge from +1 to +4, i.e., a large part of the periodic table of the elements (Hawthorne 1983; Oberti et al. 2007). Their extreme chemical variability has resulted in a relatively large number of mineralogical species and names, regulated by several IMA (International Mineralogical Association) Commissions during the last 56 years. The current nomenclature (Hawthorne et al. 2012) includes a number of root-names based on the different charge arrangements at the different structural sites, where extensive chemical variability is possible (and common).

3 The high-temperature behavior of Fe-amphiboles

The HT-behavior of Fe-bearing amphiboles involves oxidation of Fe that can be expressed as (Addison and Sharp 1962; Phillips et al. 1988; Della Ventura et al. 2018a).

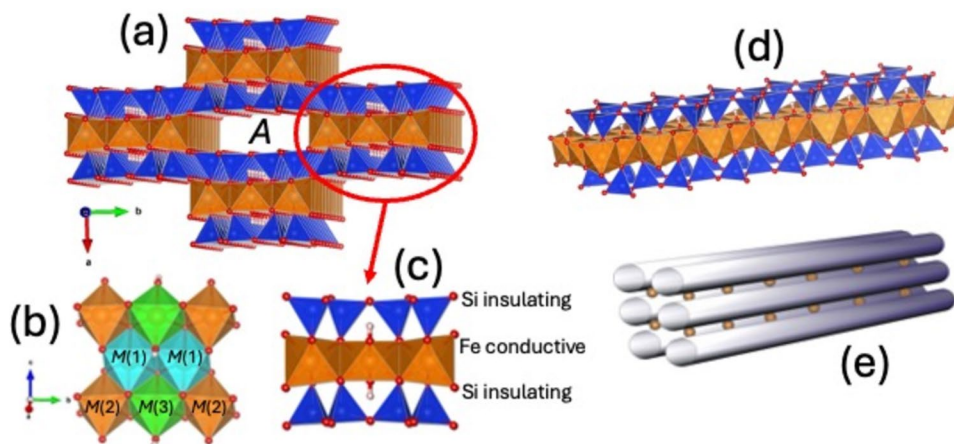


Fig. 1 **a** The structure of $C2/m$ amphiboles (drawing done with Vesta, Momma, and Izumi 2008); the single I-beam is circled, the A-site channel extending along c is indicated. **b** Nomenclature of the M-octahedra: M(1) are in cyan, M(2) in orange, and M(3) in green. **c** Particular of the I-beam module projected along c ; in riebeckite, the composition is such that a purely Fe and conductive ribbon is sand-

wiched between two silicon (insulating) double-chains, thus resulting in a kind of “electrical cable”. **d** A single I-beam extending along the c -direction, showing the nano-rod (2×1 nm) shape. **e** Schematic representation of the I-beams (gray rods) laterally connected by the M(4) sites (brown spheres) (color figure online)

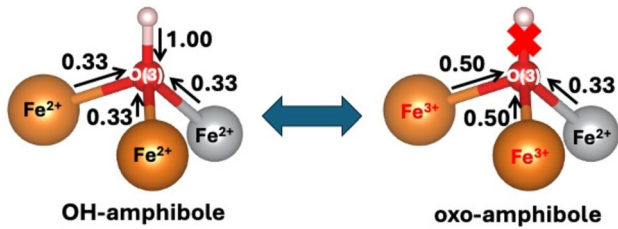
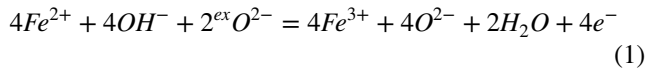


Fig. 2 The local oxidation process of Fe-amphiboles; in ideal riebeckite, only ferrous cations are ordered at the M(1)M(1)M(3) octahedra connected to the O(3) oxygen (red sphere). The ideal valence units (v.u.) converging from the NN cations toward the O(3) oxygen are indicated. Due to the local $\text{M}(1)\text{Fe}^{2+} \rightarrow \text{M}(1)\text{Fe}^{3+}$ reaction for increasing T, the bond valence on the O(3) oxygen increases and the local charge is restored by a loss of H⁺ without any structural disruption. Note that, for simplicity, the indicated v.u.s are Pauling's values not considering the effect of actual M–O bond lengths (Brown 1981). In fact, the Fe³⁺–O distance is much shorter than the Fe²⁺–O distance (Oberti et al. 2018); thus, the final charge converging on O(3) for oxo-riebeckite is higher than the one indicated in the figure (color figure online)

According to this equation, the oxidation from ferrous to ferric iron is balanced by the loss of hydrogen bonded to the O(3) oxygen (see schematic Fig. 2), which then combines at the mineral surface with external $^{\text{ex}}\text{O}^{2-}$ (if present) to produce H₂O. This is an important process in geology due to its consequences both on the thermal stability of major rock-forming silicates (*e.g.*, micas and amphiboles), and for the recycling of volatiles into the mantle. Note that a flux of electrons is also produced during Fe oxidation, a feature that has major implications for large-scale processes in the Earth's crust, as discussed in the following.

Our studies done over the last decade on different Fe-amphiboles have shown that the dehydrogenation process is not as straightforward as Eq. 1 would suggest. Oberti et al. (2016) and Della Ventura et al. (2017, 2018b) studied a synthetic potassic-ferro-richterite [nominally $^{\text{A}}\text{K}^{\text{B}}(\text{NaCa})^{\text{C}}\text{Fe}^{2+}_{5}\text{T}^{\text{Si}}\text{Si}_8\text{O}_{22}^{\text{W}}(\text{OH})_2$] and their results are summarized in Fig. 3a. The in situ evolution of the oxidation state of iron as a function of temperature was addressed via XAS spectroscopy, by fitting the pre-edge peak (Della Ventura et al. 2018b; Galdenzi et al. 2018) that is sensitive to the $\text{Fe}^{3+}/\text{Fe}^{2+}$ ratio in the mineral (*e.g.*, Giuli et al. 2003;

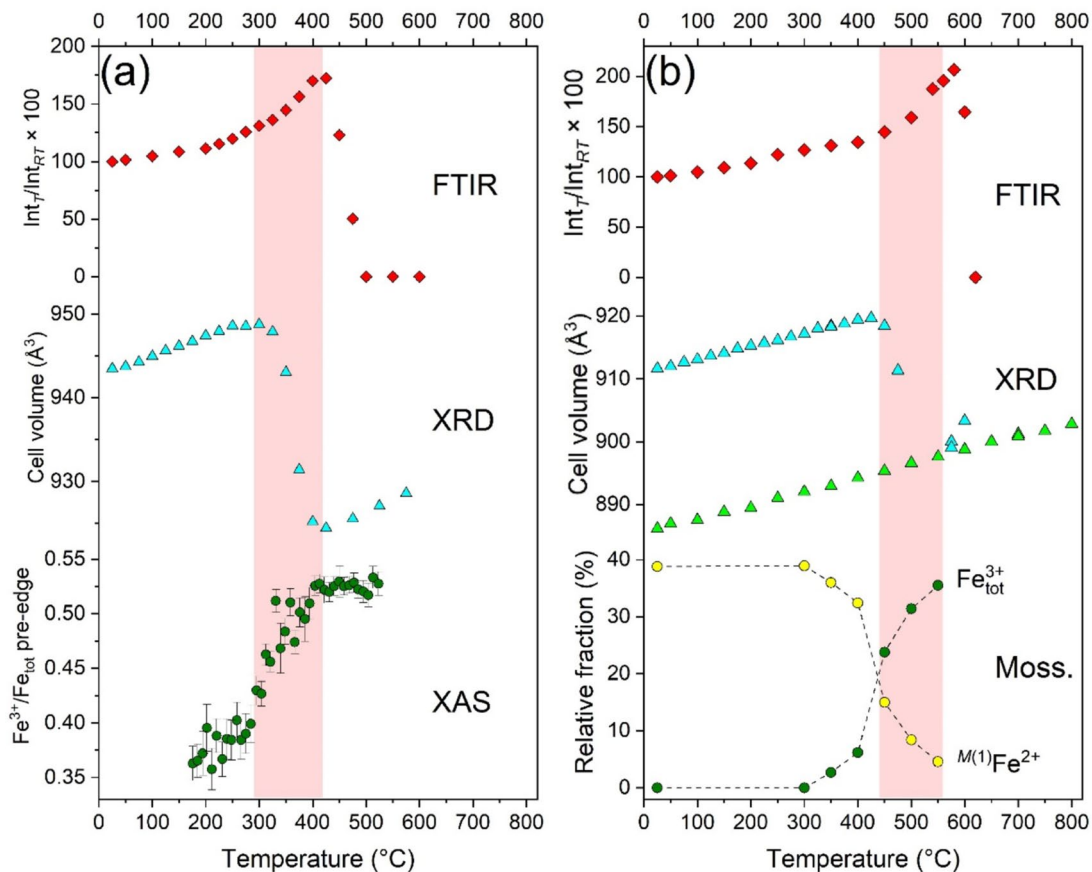


Fig. 3 **a** In situ high-T behavior of synthetic potassic-ferro-richterite, data from Oberti et al. (2016) and Della Ventura et al. (2017, 2018b). **b** In situ high-T data for riebeckite, from Della Ventura et al. (2018a) and Oberti et al. (2018)

Dyar et al. 2016; Della Ventura et al. 2024a). The data show relatively rapid Fe oxidation starting at ~ 250 °C and ending at $T > 450$ °C (Fig. 3a). In the same temperature range (red area in Fig. 3a), X-ray diffraction shows a collapse of the unit-cell volume consistent with the contraction of the octahedral ribbon due to the $\text{Fe}^{2+} \rightarrow \text{Fe}^{3+}$ transition. The loss of hydrogen was monitored by in situ HT-FTIR micro-spectroscopy on a single crystal. Interestingly, the data show an increase of the OH-stretching intensity up to the beginning of dehydrogenation, a feature that is related to the enlarged amplitudes of hydrogen displacement in the OH-stretching mode during H^+ delocalization (Della Ventura et al. 2018a). According to the IR data, loss of H^+ from the structure starts at $T = 450$ °C (Fig. 3a), suggesting that iron oxidation (which starts at ~ 250 °C) triggers H^+ expulsion from the structure. Loss of H^+ is completed 100 °C after the end of Fe oxidation, and the difference between the onset temperatures obtained by single-crystal FTIR and XRD analysis (~ 100 °C) is interpreted in terms of the different diffusion mechanisms and kinetics for H^+ and e^- required for dehydrogenation to proceed (Della Ventura et al. 2017). Refinement of *M*-site occupancies (Table 1) shows that Fe oxidation occurs exclusively at the *M*(1) site, both *M*(2) and *M*(3) sites being virtually unaffected.

Oberti et al. (2018) and Della Ventura et al. (2018a) studied a sample of riebeckite with a nearly ideal composition $[\text{ABNa}_2^{\text{C}}(\text{Fe}^{2+}_3\text{Fe}^{3+}_2)\text{T}^{\text{D}}\text{Si}_8\text{O}_{22}(\text{OH})_2]$ and their results are shown in Fig. 3b. Comparison of the data with those from potassic-ferro-richterite in Fig. 3a shows almost identical behavior, although shifted by ~ 150 °C to higher temperature.

Table 1 Refined site occupancies (apfu) for synthetic potassic-ferro-richterite before and after the thermal annealing; data from Oberti et al. (2016)

Site	Before the annealing		After the annealing	
	Fe^{2+}	Fe^{3+}	Fe^{2+}	Fe^{3+}
<i>M</i> (1)	1.81	0.19	0.25	1.75
<i>M</i> (2)	1.53	0.47	1.42	0.58
<i>M</i> (3)	0.87	0.13	0.95	0.05

Table 2 Refined site occupancies (apfu) for riebeckite before and after the thermal annealing; data from Oberti et al. (2018)

Site	Before the annealing	After the annealing
<i>M</i> (1)	0.16 Mg + 1.84 Fe^{2+}	0.05 Mg + 1.90 Fe^{3+} + 0.05 Fe^{2+}
<i>M</i> (2)	0.18 Fe^{2+} + 0.01 Zn + 0.06 Al + 1.74 Fe^{3+} + 0.01 Ti	0.09 Mg + 0.09 Fe^{2+} + 0.01 Zn + 0.06 Al + 1.74 Fe^{3+} + 0.01 Ti
<i>M</i> (3)	0.03 Mg + 0.97 Fe^{2+}	0.83 Fe^{2+} + 0.17 o
<i>M</i> (4)	1.86 Na + 0.09 Ca + 0.03 Mg + 0.02 Mn	1.10 Na + 0.09 Ca + 0.08 Mg + 0.02 Mn + 0.11 Fe^{2+} + 0.60 o
A	0.04 Na + 0.05 K	0.76 Na + 0.05 K
W	1.90 OH^- + 0.10 F^-	1.90 O^{2-} + 0.10 F^-

Based on Mössbauer spectroscopy of samples annealed at various temperatures, iron oxidation occurs mainly for $T > 400$ °C almost exclusively at the *M*(1) octahedron and is complete at $T = 650$ °C (Oberti et al. 2018); in the same temperature range, there is major contraction of the cell volume indicated by X-ray diffraction, while FTIR spectroscopy shows that H^+ loss occurs at $T > 600$ °C. Site-occupancies refined for the same crystal before and after the experiment (Table 2) show that, in accordance with Mössbauer spectroscopy, Fe oxidation occurs almost exclusively at the *M*(1) site. In addition, they show a very peculiar phenomenon of cation disordering: with increasing temperature, significant amounts of $^{\text{B}}\text{Na}$ (> 0.70 apfu) migrate from the *M*(4) to the A-site, and significant amounts of (Mg, Fe^{2+}) disorder among the *M*(1,3) and the *M*(4) site, ending with vacancies at both the *M*(3) (0.17 apfu) and *M*(4) (0.60 apfu) sites. The final product is a ribbon silicate with a partial “dioctahedral” character, a structural arrangement never observed before in amphiboles. This conclusion was supported by FTIR data collected on the sample annealed at 600 °C that gave a broad absorption centered around 3533 cm^{-1} , a wavenumber typical of dioctahedral bands in layer silicates (Robert et al. 1989; Redhammer et al. 2000; Della Ventura et al. 2024b). A similar cation disordering was also observed by Ballirano and Pacella (2020) in Fe-bearing tremolite at higher temperatures.

A notable feature that emerged from the work of Della Ventura et al. (2018a, 2024a) is that in riebeckite, the Fe oxidation is reversible over a relatively broad temperature range; up to 450 °C, both H^+ and e^- are delocalized within the crystal, and only for $T > 500$ °C, their kinetic energy is sufficiently high to allow their ejection, leading to irreversible changes in the charges at the O(3) and *M*(1) sites. This evidence was initially based on the disappearance and reappearance of Raman peaks related to Fe^{2+}O_6 and OH-stretching modes during heating–cooling experiments. It was later confirmed by a strong oscillation of the sample resistivity by orders of magnitude while cycling the temperature, indicating cyclic delocalization/relocalization of

the valence electrons during the reversible $\text{Fe}^{2+} \leftrightarrow \text{Fe}^{3+}$ exchange, in accord with a bulk process (Della Ventura et al. 2024a). Based on Raman spectroscopy, the same process has been shown to occur in other amphibole compositions, *e.g.*, grunerite (Mihailova et al. 2021) and synthetic potassic-ferro-richterite (Bernardini et al. 2024), indicating it to be a common feature of iron-rich amphiboles.

4 The thermal stability of riebeckite under different oxidizing conditions

Della Ventura et al. (2005) described the stability of magnesioriebeckite, ideally $\text{Na}_2(\text{Mg}_3\text{Fe}^{3+}_2)\text{Si}_8\text{O}_{22}(\text{OH})_2$, at 700–800 °C, 0.4 GPa, and redox conditions varying from NNO (Nickel–Nickel Oxide) to $\text{NNO} + 2.3 \log f_{\text{O}_2}$. A high (> 85%) amphibole yield was systematically obtained at these conditions. However, a combination of X-ray data, EMP analyses, Mössbauer and FTIR spectroscopies showed that the synthesized amphiboles deviated strongly from nominal stoichiometry, following a combination of the ${}^{\text{C}}(\text{Mg}, \text{Fe}^{2+})_1 {}^{\text{B}}(\text{Mg}, \text{Fe}^{2+})_1 {}^{\text{C}}\text{Fe}^{3+}_{-1} {}^{\text{B}}\text{Na}_{-1}$ and the ${}^{\text{A}}\text{Na}_1 {}^{\text{C}}(\text{Mg}, \text{Fe}^{2+})_1 {}^{\text{A}}_{-1} {}^{\text{C}}\text{Fe}^{3+}_{-1}$ exchange vectors, pointing to an inverse relationship between A-site occupancy and oxygen fugacity, in accord with data from natural occurrences.

Early experiments on the behavior of riebeckite during thermal treatment under different oxidizing conditions have been reported by Hodgson et al. (1965) and Whitfield and Freeman (1967) who observed the appearance at 500–600 °C under N_2 atmosphere of a modified amphibole phase named “crocidolite anhydrite”, the structural details of which could not be determined. Della Ventura et al. (2023) addressed the stability of riebeckite annealed at different temperatures in air *vs.* vacuum. The run products were studied by Mössbauer spectroscopy and powder X-ray diffraction and showed that riebeckite may follow two distinct paths depending on the external environment. Under oxidizing conditions, it is stable in the hydrous form up to relatively low temperatures (400–450 °C), and then, it undergoes dehydrogenation in a narrow T interval (within ~ 50 °C) forming oxo-riebeckite which is stable up to ~ 900 °C. The final break-down products of oxo-riebeckite include aegirine + cristobalite + hematite. Based on the relative intensity of the (310) Bragg reflection, the activation energy (E_a) for the riebeckite → oxo-riebeckite transition was found to be 166 ± 6 kJ/mol. Interestingly, the activation energy obtained by X-ray diffraction for powdered riebeckite was the same (within experimental errors) as that obtained by FTIR spectroscopy, indicating that the structure adjustment due to Fe oxidation (probed by XRD) and H^+ diffusion (probed by FTIR) have similar energetics (Della Ventura et al. 2023). Under vacuum conditions, no Fe oxidation is observed, and riebeckite is stable up to much higher temperatures (750–800 °C).

However, in the range $550 < T < 700$ °C, it undergoes significant rearrangement of the C-cations whereby the amphibole stable in the 700–800 °C range has the same chemical formula as riebeckite, but has a disordered and non-standard cation distribution on the ribbon of octahedra: $M^{(1)}(\text{Fe}^{3+}\text{Fe}^{2+})M^{(2)}(\text{Fe}^{3+}\text{Fe}^{2+})M^{(3)}\text{Fe}^{2+}$ (Fig. 4). This phase was termed “ CR^{3+} disordered riebeckite” by Della Ventura et al. (2023). For $T \geq 800$ °C, the mineral decomposes to aegirine + fayalite + cristobalite + H_2O .

In conclusion, Della Ventura et al. (2023) demonstrated that the presence of external oxygen determines the temperature at which H_2O is released into the surrounding system. Another important petrological implication of the results of the work of Della Ventura et al. (2023) is that characterization of the oxidation state of iron in the amphibole does not necessarily provide the redox conditions of equilibration if site occupancies for Fe are not determined.

5 The kinetics of H^+ diffusion in riebeckite

The kinetics of HT dehydrogenation of riebeckite was addressed via isothermal experiments on both powders and single crystals up to 560 °C by monitoring the O–H stretching signal via Fourier Transform Infrared (FTIR) spectroscopy (Della Ventura et al. 2022). Experiments in air

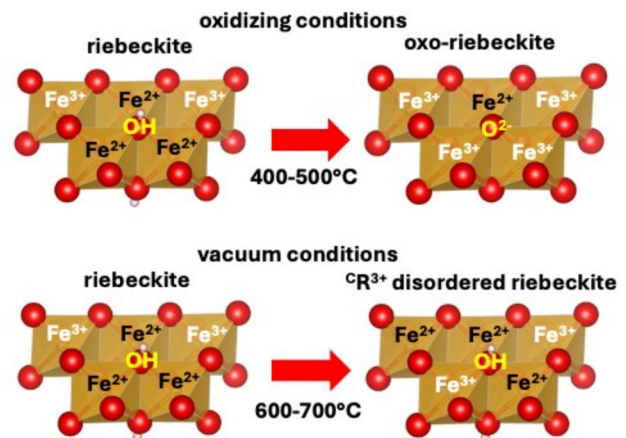


Fig. 4 Schematic site distribution for riebeckite after high-temperature experiments. Above: local transition at the M(1–3) octahedra in oxidizing (air) atmosphere; two M(1)Fe²⁺ + oxidize at 400–450 °C into M(1)Fe³⁺ + cations and the H⁺ ion is lost. In these conditions, water is released at low temperature into the surroundings. Below: local transition at the M(1–3) octahedral sites in vacuum; no M(1)Fe²⁺ oxidation occurs; however, in the 600–700 °C range, there is a cation rearrangement toward CR³⁺-disordered riebeckite. Note that at these conditions, the local charge arrangement around the O–H group is similar to amphiboles like pargasite and does not require the H⁺ loss (see Della Ventura et al. 1999). In these conditions, water is released into the surroundings only after the structure disruption, for $T > 750$ °C

on pellets of pure amphibole powder or finely ground amphibole embedded in a KBr matrix revealed a rapid decrease of the OH-stretching IR absorbance with increasing temperature up to 520 °C for pure riebeckite powder, indicating progressive dehydrogenation. In contrast, the same powder pelletized into KBr did not show any H⁺ loss even after prolonged heating (> 180 min). This result may be explained by considering that KBr acts as an envelope preventing contact between the mineral powder and the air during the thermal ramp. Thus, neither Fe oxidation nor H⁺ loss could occur in amphibole particles embedded in a KBr matrix, and subsequent experiments with powders were done using pure mineral disks (Della Ventura et al. 2023).

An exponential decrease of the OH-stretching intensity as a function of time during different isothermal experiments was obtained for pure powders (Fig. 5a), whereas data collected on single crystals (Fig. 5b) showed an initial increase in IR absorption intensity due to increasing vibrational amplitudes of the O–H bond-stretching and proportional to the kinetic energy necessary to activate H⁺ mobilization. Based on work done on similar substances (see Della Ventura et al. 2022 for a complete list of references), the OH-intensities vs. time were fitted using the formalism for first-order reactions. Different activation energies for H⁺ diffusion were obtained for powders (159 ± 15 kJ/mol) and for single crystals (216 ± 20 kJ/mol). The larger activation energy obtained for single crystals can be understood by considering that single-crystal specimens have dimensions 1–2 orders of magnitude larger than those of the small crystalline grains in a powder. Consequently, dehydrogenation of single crystals should not be a pure first-order reaction as it involves two processes: (1) delocalization and (2) diffusion of H⁺ through the mineral (Della Ventura et al. 2022). Interestingly, synchrotron-radiation FTIR imaging suggests

that H⁺ diffusion occurs mainly perpendicular to the silicate ribbon. The results of the work of Della Ventura et al. (2022) confirmed that the release of H⁺ from riebeckite occurs after the irreversible Fe²⁺-to-Fe³⁺ exchange at temperatures > 550 °C. In addition, their work confirmed that the release of H⁺ ions from the mineral needs the presence of external oxygen that, by interacting with H⁺ at the crystal surface, triggers the formation of H₂O molecules. Hence, oxidizing conditions are required for the amphibole to be an efficient water carrier at depth at temperatures well below its break-down conditions, a feature that has paramount implications for the water cycling in the Earth's interior.

6 Electrical conduction in amphiboles

Early experimental studies on electrical conduction in Fe-rich amphiboles were done by Littler and Williams (1965), Tolland (1973), and Parkomenko (1982) who reported resistivity data on samples with a broad range of composition. Schmidbauer et al. (1996, 2000) later examined single crystals of both sodium- and calcium-amphiboles by combining impedance and Mössbauer spectroscopies, both in air and in N₂ atmosphere. Because of the low activation energy (< 1 eV), they proposed the hopping of Fe electrons as the conduction mechanism; notably, they observed the conductivity along [001] to be five-to-six times larger than that perpendicular to [001]. Small-polaron conduction (*i.e.*, electron hopping between ^CFe²⁺ and ^CFe³⁺) as the main mechanism responsible in Fe-amphiboles was also postulated by Wang et al. (2012) for hornblende-rich rocks and by Hu et al. (2018) for edenite single crystals examined at high-T and -P conditions. More recently, Shen et al. (2020) observed an abrupt rise in conductivity in single crystals of

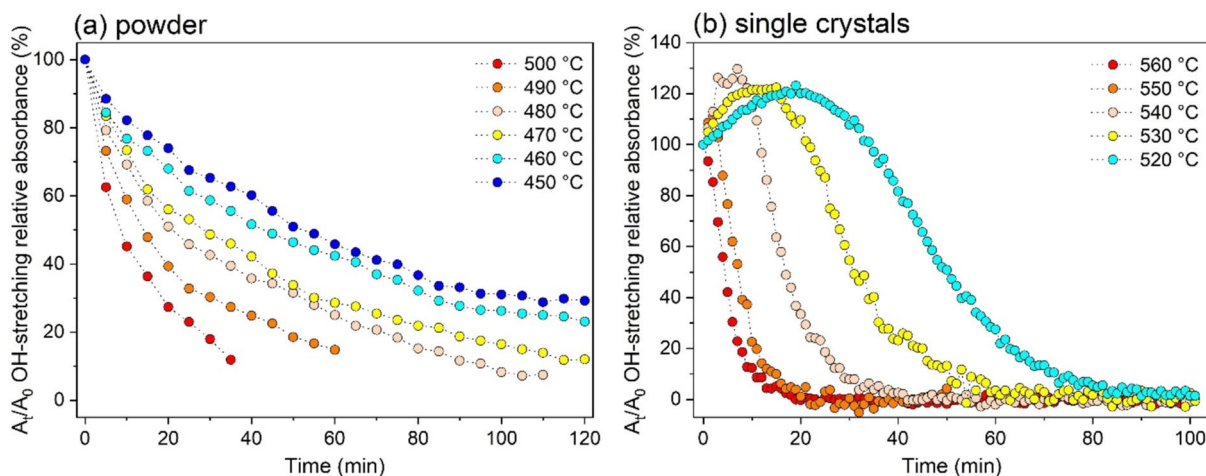


Fig. 5 Relative intensity of the OH-stretching absorbance (A_t/A_0 , %) as a function of time during isothermal experiments on **a** pure powder pellets, and **b** doubly polished single crystals. Modified from Della Ventura et al. (2022)

Fe-free tremolite at $T > 900$ °C. The activation energy of the enhanced conductivity was 365 kJ/mol (3.79 eV), much higher than the values measured for Fe-bearing amphiboles, implying a different conduction mechanism such as ion (Mg^{2+} , Ca^{2+}) diffusion (Katsura et al. 2009; Shen et al. 2020). A selection of data from the literature (single-crystal data only) is given in Table 3; two points are worth noting: (1) both *dc* measurements and impedance spectroscopy yield similar E_a values; for $\text{Fe}/(\text{Fe} + \text{Mg}) > 0.2$ apfu, E_a is systematically < 1 eV. (2) The amphibole composition, in particular the Fe content, has a significant effect on the measured conduction (see Parkomenko 1982 and Della Ventura et al. 2024a).

Direct and robust proof for the activation of anisotropic electron–phonon excitations (polarons) in Fe-bearing amphiboles has been provided only recently by Mihailova et al. (2021) via direction-dependent resonance Raman scattering (RRS). In insulating or semiconducting materials such as amphiboles, electron–phonon coupling occurs via Fröhlich interactions (Yu and Cardona 2010), *i.e.*, electrostatic

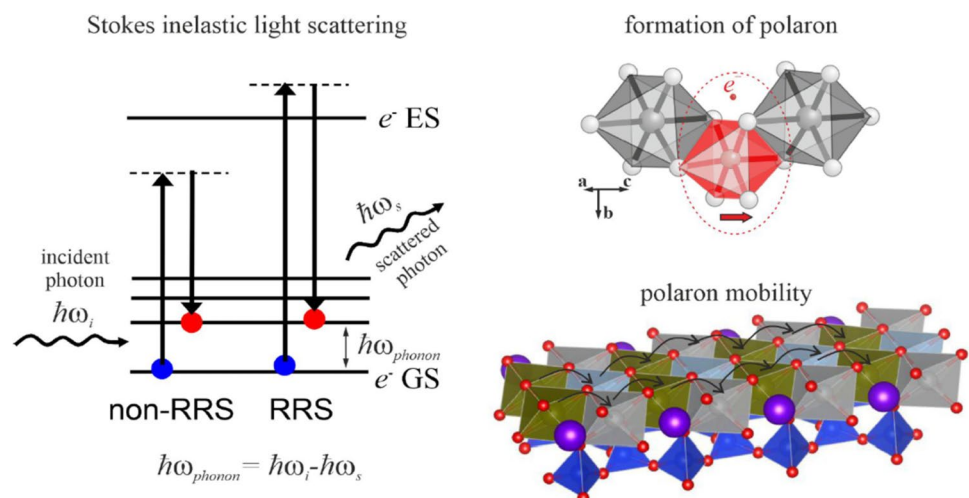
interactions between delocalized electrons (*i.e.*, electrons in the conduction band) and longitudinal optical (LO) polar phonons (*i.e.*, wave-like disturbances propagating throughout the structure). The LO phonons arise from the modulated change in size of the $(\text{Fe}^{2+}, \text{Fe}^{3+})\text{-O}$ octahedra due to the itinerant electrons causing cycling change of the Fe-ion radii (Figs. 6b, c). Under these conditions, the photon from the laser beam interacts with both the phonon and the electron (Merlin et al. 2000; Yu and Cardona 2010) and the symmetry selection rules are modified: the polar optical modes related to the atomic species in which the electron transition occurs (in our case the Fe–O modes) are enhanced, whereas those related to the other atomic species are suppressed (de la Flor et al. 2014). In centrosymmetric crystals such as amphiboles, the normally Raman-active modes are non-polar and, therefore, they will be suppressed under resonance conditions, while normally infrared-active modes will be enhanced. The first evidence of strongly anisotropic Fe-related polarons in amphiboles came from in situ high-temperature experiments on grunerite [ideally $\text{Fe}_7\text{Si}_8\text{O}_{22}(\text{OH})_2$]

Table 3 Selected conductivity data for single-crystal amphiboles as found in the literature (from Della Ventura et al. 2024a)

E_a (eV)	Method	Sample identification	Fe/(Fe + Mg)	Reference
0.69	dc electrical resistance	riebeckite (crocidolite)	Close to 1.0*	Littler and Williams (1965)
0.54 // c; 0.57 \perp c	dc electrical resistance	Not given	0.19	Tolland (1973)
0.9 for $T > 800$ °C	dc electrical resistance	riebeckite	Close to 1.0*	Parkomenko (1982)
0.4	Impedance spectroscopy	arfvedsonite	1.0	Schmidbauer et al. (1996)
0.73–1.06	Impedance spectroscopy	Sample A1 magnesio-hornblende	0.22	Schmidbauer et al. (2000)
0.58	Impedance spectroscopy	Sample A2 ferro-edenitic-hornblende	0.75	Schmidbauer et al. (2000)
0.61	Impedance spectroscopy	Sample A3 kaersutite	0.25	Schmidbauer et al. (2000)
0.70–0.80	Impedance spectroscopy	edenite	0.36	Hu et al. (2018)
3.79	Impedance spectroscopy	tremolite	Close to 0.01	Shen et al. (2020)
0.77	dc electrical resistance	riebeckite	0.95	Della Ventura et al. (2024a)

* Not known, assumed

Fig. 6 **a** Energy-level diagram of photon inelastic light scattering and sketches of **b** the formation of hopping electrons and **c** of polarons along the structural I-beams of the amphibole structure. e-GS and e-ES are the electronic ground and excited states, respectively (after Bernardini et al. 2023)



using parallel polarized backscattering geometry (Mihailova et al. 2021). The results (Fig. 7) show that when $\mathbf{E}_i \perp \mathbf{c}$ (the electrical vector of the laser perpendicular to the \mathbf{c} -axis of the amphibole), all Raman-active phonon modes are well preserved up to high-T (see Fig. 7a), whereas when $\mathbf{E}_i \parallel \mathbf{c}$ the OH-stretching peaks and all vibrational modes associated with the TO_4 ribbons disappear above 477 °C (see the red spectrum in Fig. 7b) and a strong peak due to RRS appears near 576 cm^{-1} (RRS in Fig. 7b) (Mihailova et al. 2021). Hence, the complete change in the Raman selection rules observed when the amphibole crystal is oriented with the \mathbf{c} -axis $\parallel \mathbf{E}_i$ unambiguously demonstrates the formation of polarons with dipoles parallel to the TO_4 - MO_6 ribbons (*i.e.*, an electron flux along the I-beam, Fig. 6c).

For grunerite, the activation of polarons was also supported by DOS (density-of-state) calculations showing that the top of the valence band and the bottom of the conduction band are exclusively formed from hybridized electron states of octahedrally coordinated Fe^{2+} cations and adjacent O^{2-} anions. The value calculated for the energy gap $E_g = 0.05$ eV is in excellent agreement with the observed temperature of RRS appearance (~ 427 °C) during the experiments, corresponding to 0.06 eV (Mihailova et al. 2021).

The first direct proof for the formation of strongly anisotropic polarons in Fe-amphiboles provided by Mihailova et al. (2021) opened a new frontier for in situ

high-temperature Raman spectroscopy, now considered an efficient tool to study thermally activated charge carriers in complex hydrous silicates. Conductivity, a fundamental macroscopic physical property of rock-forming minerals, is typically studied via resistivity measurement or complex impedance spectroscopy (see Table 3) which cannot provide any information on the atomic-scale mechanism of the process. The work of Mihailova et al. (2021) demonstrates that the response to temperature of iron-bearing minerals, in terms of charge-carrier mobility, can be effectively addressed via relatively easy-to-handle Raman scattering measurements. Certainly, Raman spectroscopy does not allow quantifying the electrical conductivity but allows constraining both its type (*i.e.*, polaronic *vs.* ionic) and the temperature of activation and stability of charge carriers. This information can be combined with the conductivity data available in the literature for a wide spectrum of rock-forming minerals (*e.g.*, Karato and Wang 2013; Yoshino and Karsura 2013; Dai et al. 2020) to support the geophysical models derived from magnetotelluric measurements.

More recently, the appearance of RRS in actinolite (Rösche et al. 2023) revealed that even small amounts of Fe in essentially magnesian amphiboles are sufficient to trigger the formation of polaronic conduction, although at much higher temperatures than in Fe-rich amphiboles (Mihailova et al. 2022). Moreover, the presence of A-site cations reduces

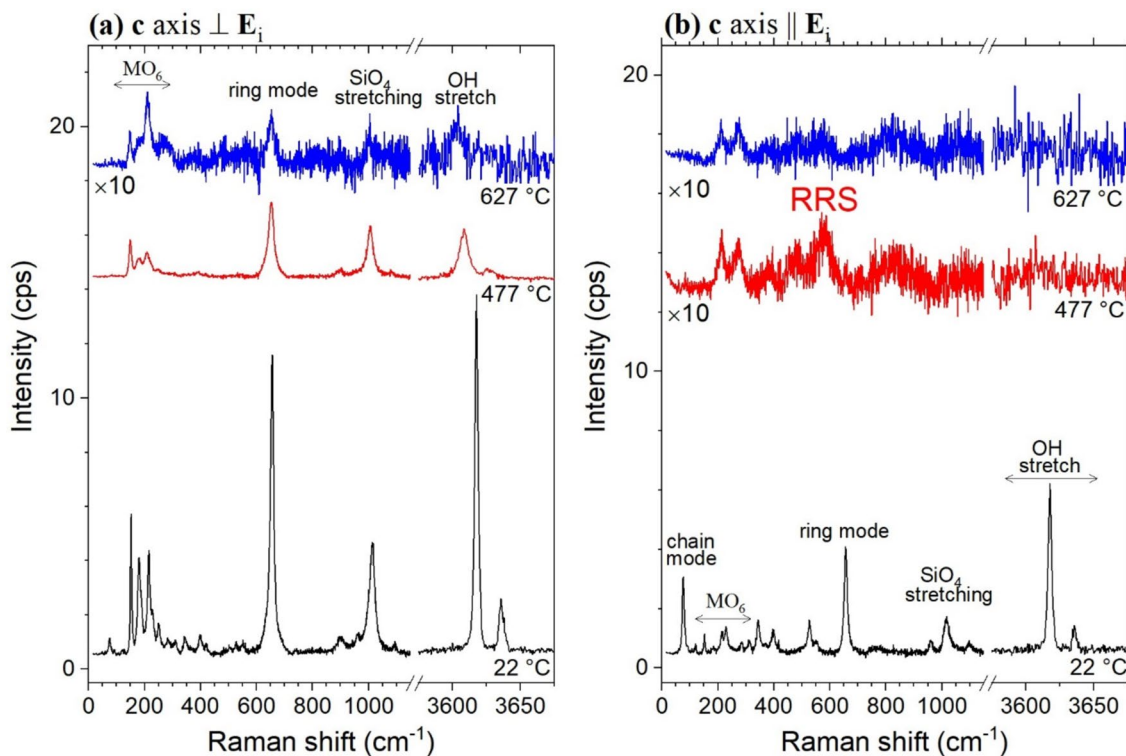


Fig. 7 Temperature-dependent polarized Raman spectra of grunerite measured in situ in air in different scattering geometries: **a** with the \mathbf{c} -axis $\perp \mathbf{E}_i$ (polarization of the incident light) and **b** with the \mathbf{c} -axis $\parallel \mathbf{E}_i$. RRS: resonance Raman scattering. Modified from Mihailova et al. (2021)

the activation temperature of mobile polarons and delocalized H^+ ions (Bernardini et al. 2024).

7 Implications

Thermally activated redox processes in minerals induce electron cycling and are thus expected to contribute to lithospheric conductivity, the ultimate origin of which is still poorly understood quantitatively at the atomic scale (Fullea et al. 2011; Evans et al. 2014). Anomalous high-conductivity layers (HCL) are characteristics of subduction zones thanks to magnetotelluric (MT) measurements in different areas of the Earth, *e.g.*, Bolivia, Costa Rica, Greece, Mariana, Mexico New Zealand, and Perù/Chile (Pommier 2014; Syracuse et al. 2010). The constituent metamorphic rocks typically contain Fe-rich silicates such as amphiboles and micas. Two main mechanisms have been proposed to explain the geophysical data: (1) ionic conductivity of aqueous fluids

at mineral-grain boundaries, formed as a result of metamorphic/metasomatic processes (Manthilake et al. 2016; Hu et al. 2017), and (2) the inherent conductivity of minerals (Wang et al. 2012, 2013; Li et al. 2016; Hu et al. 2018). However, recent studies have shown that fluids alone cannot explain the anomalously high anisotropic conductivity in the mantle wedge (Yoshino et al. 2006) and this evidence has triggered increasing scientific interest in the mechanism of formation of intrinsic charge carriers in rock-forming minerals (*e.g.*, Katsura et al. 2009), particularly in Fe-bearing amphiboles (see Della Ventura et al. 2024a for a complete list of references).

Bernardini et al. (2023) compared the temperature ranges of polaron stability in the model compound riebeckite, experimentally determined via RRS, with the thermal profiles for two “end-member” subduction zones (hot and cold) located in the same geographic area (Japan, Fig. 8a). The important conclusion of this work is that the large-scale conductivity found by MT measurements (Kasaya et al.

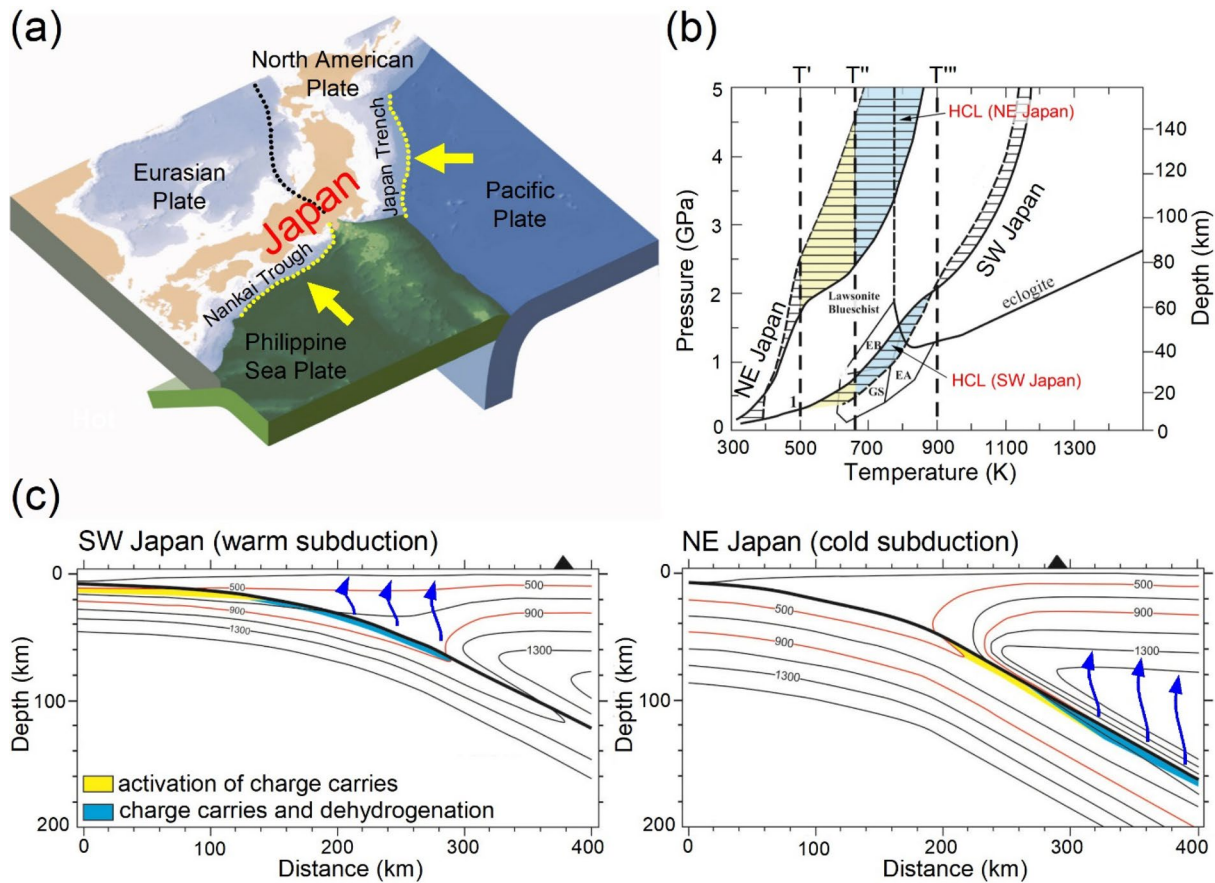


Fig. 8 **a** Schematic subduction of the Philippine Sea plate (warm subduction) and of the Pacific Plate (cold subduction) beneath the Japan Islands (modified after Lin et al. 2016); **b** P–T conditions for the activation of charge carriers and dehydrogenation NE and SW Japan; the stability P–T area for eclogite, lawsonite-blueschist, epidote blueschist (EB), epidote amphibolite (EA), and greenschist (GS) facies

rocks is also indicated (modified after Peacock and Wang 1996); **c** Temperature-activated charge carriers and dehydrogenation in different subduction zone settings. Calculated thermal structure for (a) SW and (b) NE Japan subduction zones. Blue arrows: ascending of the fluids released during the amphibole dehydrogenation (modified from Bernardini et al. 2023)

2005; Ichiki et al. 2015) can be accurately interpreted by considering the response of the amphibole to the conditions (geothermal gradient) imposed by the thermal structure of the downgoing slab. In this connection, it is also important to emphasize that the conductivity of (Fe–Mg)-amphiboles is orders of magnitude greater than that of most other rock-forming minerals such as chlorite ($\sim 10^{-5}$ S/m: Manthilake et al. 2016), epidote ($\sim 10^{-3}$ S/m: Hu et al. 2017), plagioclase ($< 10^{-8}$ S/m: Yang et al. 2012), and quartz ($\sim 10^{-5}$ S/m, Wang et al. 2002), suggesting that amphiboles have a major role in determining the electrical properties of the descending plate.

The thermal structure at depth in the study area (NE and SW Japan) is given in Fig. 8b (modified from Peacock and Wang 1996) where the vertical broken lines indicate the temperatures for the onset of activation of small polarons (T'), for the completion of small polarons and H^+ delocalization (T''), and for the completion of amphibole dehydrogenation (T'''). As discussed by Bernardini et al. (2023), oceanic crust subducting beneath southwest Japan (hot subduction conditions) passes through the greenschist and epidote/amphibolite/blueschist facies and enters the eclogite facies at a depth of ~ 50 km (Fig. 8b); the activation of charge carriers is expected for a depth > 15 km, where $T > T'$ (Fig. 8b). In this area, an HCL develops between 15 and 30 km in depth (Kasaya et al. 2005) where temperatures correspond to those of the $T'–T''$ interval. For conditions between the T'' and T''' , H^+ mobility further contributes to the charge carriers; a low seismic-velocity layer is also known to extend to 60 km, which is the maximum depth of intraslab earthquakes (e.g., Hori 1990). The shallow release of water occurring at the SW Japan conditions (see schematic Fig. 8c) is thus in agreement with the scarce volcanism and the generation of mega earthquakes in this area (Kasaya et al. 2005).

On the other hand, oceanic crust subducting beneath north-eastern Japan (cold subduction conditions) passes through the lawsonite-blueschist facies and enters the eclogite facies at a depth of 110 km (Fig. 8b); in this area, a low-velocity layer extends to 150 km and intraslab earthquake activity extends to 200 km in depth (Hasegawa et al. 1994). Inspection of Fig. 8b shows that polaronic conductivity in amphibole-bearing rocks is expected at the top of the oceanic crust only from ~ 60 km depth, again in accord with geophysical measurements (Ichiki et al. 2015). Under these conditions, amphibole dehydrogenation is expected to occur at depths > 80 km (Fig. 8c), thus promoting a deep conductivity anomaly, deep intraslab earthquakes, and the production of voluminous magmatism as it is observed in this area (Kimura and Nakajima 2014).

In summary, although our model is extremely simplified being based on data collected for a single mineral and for a single composition, we observed an astonishing match between the expected depths of development of conductivity and dehydrogenation for our model amphibole

and those of the geophysical discontinuities (HCLs, low seismic-velocity layers, and the maximum depth of water-triggered intraslab earthquakes) inferred from MT measurements.

8 Conclusions and further work

During the last decade, we have extensively studied the behavior of Fe-rich amphiboles at high temperatures using a multi-technique approach. We discovered that what was considered a simple oxidation reaction is actually a complex and dynamical process, reversible in a relatively large T interval, an unknown feature that has major implications for Petrology, Geophysics, and Material Science. Our Raman scattering experiments show that, for temperatures above a certain threshold, amphiboles behave as semiconductors, having mobile charge carriers in the bulk crystal, *i.e.*, delocalized e^- coupled with phonons to form polarons as well as delocalized H^+ ions. The activation temperature of charge carriers, the temperature range of their existence before being ejected from the bulk crystal, and the magnitude and degree of alignment of polaron dipole-moments depend significantly on the amphibole crystal chemistry (Mihailova et al. 2021, 2022; Bernardini et al. 2023, 2024; Rösche et al. 2023). There is strong evidence, indicating that electrical anomalies are associated with different large-scale and important geological processes like water cycling, volcanism, seismicity, and ore generation. Therefore, an improved insight into the physical properties at high temperatures and pressures of common rock-forming minerals, such as amphiboles, pyroxenes, and layer silicates, is mandatory for quantitative modeling of large-scale deep-Earth processes.

Our work definitively demonstrates that Raman spectroscopy, being sensitive to both electron and phonon excitations, may provide straightforward access to these processes via systematic examination of all relevant rock-forming minerals.

Acknowledgements Financial support by the Deutsche Forschungsgemeinschaft (MI 1127/7-2) as well as by the Grant to Department of Science, Roma Tre University (MIUR-Italy Dipartimenti di Eccellenza, ARTICOLO 1, COMMI 314-337 LEGGE 232/2016) is gratefully acknowledged. FCH was supported by a Discovery Grant from the Natural Sciences and Engineering Council of Canada. Gianluca Iezzi (Chieti) and an anonymous referee provided useful suggestions to improve our work.

Author contribution GDV presented the work and wrote the preliminary draft of the paper. SB prepared the figures. All authors reviewed the manuscript.

Data availability No datasets were generated or analysed during the current study.

Declarations

Conflict of interest The authors declare no competing interests.

References

- Addison WE, Sharp JH (1962) Amphiboles. Part III. The reduction of crocidolite. *J Chem Soc* 34:3693–3698
- Addison WE, White AD (1968) The oxidation of bolivian crocidolite. *Min Mag* 36:791–796
- Addison CC, Addison WE, Neal GH, Sharp JH (1962a) Amphiboles. Part I. The oxidation of crocidolite. *J Chem Soc.* <https://doi.org/10.1039/jr9620001468>
- Addison WE, Neal GH, Sharp JH (1962b) Amphiboles Part II. The kinetics of oxidation of crocidolite. *J Chem Soc.* <https://doi.org/10.1039/jr9620001472>
- Addison WE, Sharp JH (1968) Redox behavior of iron in hydroxylated silicates. Eleventh Conference on Clays and Clay Minerals. Abstracts. pp 95–104.
- Aines RD, Rossman GR (1985) The high temperature behaviour of trace hydrous components in silicate minerals. *Am Mineral* 70:1169–1179
- Ballirano P, Pacella A (2020) towards a detailed comprehension of the inertisation processes of amphibole asbestos: in situ high-temperature behaviour of fibrous tremolite. *Min Mag* 84:888–899
- Bernardini S, Della Ventura G, Schlüter J, Mihailova B (2023) Thermally activated electron hopping in Fe-rich amphiboles: implications for the high-conductivity anomalies in subduction zones. *Geochem* 83:125942. <https://doi.org/10.1016/j.chemer.2022.125942>
- Bernardini S, Della Ventura G, Schlüter J, Hawthorne FC, Mihailova B (2024) The effect of A-site cations on the charge-carrier mobility in Fe-bearing amphiboles. *Am Mineral.* <https://doi.org/10.2138/am-2023-9138>
- Brown ID (1981) The bond-valence method: an empirical approach to chemical structure and bonding. In: O'Keeffe M, Navrotsky A (eds) *Structure and Bonding in Crystals*. Academic Press, New York, pp 1–30
- Cámara F, Oberti R, Della Ventura G, Welch MD, Maresch WV (2004) The crystal structure of synthetic $\text{NaNa}_2\text{Mg}_5\text{Si}_8\text{O}_{21}(\text{OH})_3$, a triclinic C-1 amphibole with a triple cell and excess hydrogen. *Am Mineral* 89:1464–1473
- Dai L, Hu H, Jiang J, Sun W, Li H, Wang M, Vallianatos F, Saltas V (2020) An overview of the experimental studies on the electrical conductivity of major minerals in the upper mantle and transition zone. *Materials* 13:408. <https://doi.org/10.3390/ma13020408>
- de la Flor G, Wehber M, Rohrbeck A, Aroyo MI, Bismayer U, Mihailova B (2014) Resonance Raman scattering of perovskite-type relaxor ferroelectrics under non-ambient conditions. *Phys Rev B* 90:064107. <https://doi.org/10.1103/PhysRevB.90.064107>
- Deer WA, Howie RA, Zussman J (1997) *Double-chain silicates*, 2nd edn. The Geological Society, London
- Della Ventura G, Hawthorne FC, Robert J-L, Delbove F, Welch MD, Raudsepp M (1999) Short-range order of cations in synthetic amphiboles along the richterite - pargasite join. *Eur J Mineral* 11:79–94
- Della Ventura G, Iezzi G, Redhammer GJ, Hawthorne FC, Scaillet B, Novembre D (2005) Synthesis and crystal-chemistry of alkali amphiboles in the system $\text{Na}_2\text{O}-\text{MgO}-\text{FeO}-\text{Fe}_2\text{O}_3-\text{SiO}_2-\text{H}_2\text{O}$ as a function of f_{O_2} . *Am Mineral* 90:1375–1383
- Della Ventura G, Radica F, Bellatreccia F, Freda C, Cestelli-Guidi M (2015a) Speciation and diffusion profiles of H_2O in water-poor beryl: comparison with cordierite. *Phys Chem Mineral* 42:735–745
- Della Ventura G, Radica F, Bellatreccia F, Cavallo A, Cinque G, Tortora L, Behrens H (2015b) FTIR imaging in diffusion studies: CO_2 and H_2O in a synthetic sector-zoned beryl. *Front Earth Sci.* <https://doi.org/10.3389/feart.2015.00033>
- Della Ventura G, Susta U, Bellatreccia F, Marcelli A, Redhammer G, Oberti R (2017) Deprotonation of Fe-dominant amphiboles: Single-crystal HT-FTIR spectroscopic studies of synthetic potassic-ferro-richterite. *Am Mineral* 102:117–125
- Della Ventura G, Mihailova B, Susta U, Cestelli-Guidi M, Marcelli A, Schlüter J, Oberti R (2018a) The dynamics of Fe oxidation in riebeckite: a model for amphiboles. *Am Mineral* 103:1103–1111. <https://doi.org/10.2138/am-2018-6382>
- Della Ventura G, Galdenzi F, Cibin G, Oberti R, Xu W, Macis S, Marcelli A (2018b) Iron oxidation dynamics vs. temperature of synthetic potassic-ferro-richterite: a XANES investigation. *Phys Chem Chem Phys* 20:21764–21771. <https://doi.org/10.1039/C8CP04249G>
- Della Ventura G, Radica F, Galdenzi F, Susta U, Cinque G, Mihailova B, Marcelli A (2022) Kinetics of hydrogen diffusion in riebeckite, $\text{Na}_2\text{Fe}^{3+}_2\text{Fe}^{2+}_3\text{Si}_8\text{O}_{22}(\text{OH})_2$: an HT-FTIR study. *Am Mineral* 107:754–764. <https://doi.org/10.2138/am-2022-8021>
- Della Ventura G, Redhammer GJ, Galdenzi F, Ventruti G, Susta U, Oberti R, Radica F, Marcelli A (2023) Oxidation or cation rearrangement? Distinct behavior of riebeckite at high temperature. *Am Mineral* 108:59–69. <https://doi.org/10.2138/am-2022-8073>
- Della Ventura G, Galdenzi F, Marcelli A, Cibin G, Oberti R, Hawthorne FC, Bernardini S, Mihailova B (2024a) In situ simultaneous Fe K-edge XAS spectroscopy and resistivity measurements of riebeckite: implications for anomalous electrical conductivity in subduction zones. *Geochem* 84:126037. <https://doi.org/10.1016/j.chemer.2023.126037>
- Della Ventura G, El Moutouakkil N, Boukili B, Bernardini S, Sodo A, Cestelli-Guidi M, Holtz F, Lucci F (2024b) Tracking the Ti^{4+} substitution in phlogopite by spectroscopic imaging: a tool for unravelling the growth of micas at high pressure/temperature. *Geosci Frontiers.* <https://doi.org/10.1016/j.gsf.2024.101777>
- Dyar MD, Breves EA, Gunter ME, Lanzirotti A, Tucker JM, Carey CJ, Pee SE, Brown EB, Oberti R, Lerotic M, Delaney JS (2016) Use of multivariate analysis for synchrotron micro-XANES analysis of iron valence state in amphiboles. *Am Mineral* 101:1171–1189
- Ernst WG, Wai M (1970) Mössbauer, infrared, X-ray and optical study of cation ordering and dehydrogenation in natural and heat-treated sodic amphiboles. *Am Mineral* 55:1226–1258
- Evans RL, Wannamaker PE, McGary RS, Elsenbeck J (2014) Electrical structure of the central cascadia subduction zone: the EMSLAB Lincoln line revisited. *Earth Planet Sci Lett* 402:265–274
- Fullea J, Muller MR, Jones AG (2011) Electrical conductivity of continental lithospheric mantle from integrated geophysical and petrological modeling: Application to the Kaapvaal craton and rehotob terrane, southern Africa. *J Geophys Res* 116:B10202. <https://doi.org/10.1029/2011JB008544>
- Galdenzi F, Della Ventura G, Cibin G, Macis S, Marcelli A (2018) Accurate $\text{Fe}^{3+}/\text{Fe}_{\text{tot}}$ ratio from XAS spectra at the Fe K-edge. *Radiation Phy Chem* 1:1–4. <https://doi.org/10.1016/j.radphyschem.2018.12.008>
- Giuli G, Paris E, Pratesi G, Koeberl C, Cipriani C (2003) Iron oxidation state in the Fe-rich layer and silica matrix of Libyan desert glass: a high-resolution XANES study. *Meteorit Planet Sci* 38:1181–1186
- Gunter ME, Belluso E, Mottana A (2007) Amphiboles: Environmental and health. *Rev Mineral Geochem.* <https://doi.org/10.2138/rmg.2007.67.12>
- Hasegawa A, Horiuchi S, Umino N (1994) Seismic structure of the northeastern Japan convergent margin: a synthesis. *J Geophys Res* 99:22295–22311. <https://doi.org/10.1029/93JB02797>
- Hawthorne FC (1983) The crystal chemistry of the amphiboles. *Can Mineral* 21:173–480

- Hawthorne FC, Oberti R (2007) Amphiboles: Crystal-chemistry. *Rev Mineral Geochem* 67:1–54
- Hawthorne FC, Oberti R, Ungaretti L, Grice JD (1996) A new hypercalcic amphibole with Ca at the a site: fluor-cannilloite from pargas, finland. *Am Mineral* 81:995–1002
- Hawthorne FC, Oberti R, Harlow GE, Maresch WV, Martin RF, Schumacher JC, Welch MD (2012) Nomenclature of the amphibole supergroup. *Am Mineral* 97:2031–2048
- Hodgson AA, Freeman AG, Taylor HFV (1965) The thermal decomposition of crocidolite from Koegas, South Africa. *Mineral Mag* 35:5–29
- Hori S (1990) Seismic waves guided by untransformed oceanic crust subducting into the mantle: the case of the Kanto district, Central Japan. *Tectonophysics* 176:355–376. [https://doi.org/10.1016/0040-1951\(90\)90078-M](https://doi.org/10.1016/0040-1951(90)90078-M)
- Hu H, Dai L, Li H, Hui K, Sun W (2017) Influence of dehydration on the electrical conductivity of epidote and implications for high-conductivity anomalies in subduction zones. *J Geophys Res Solid Earth* 122:2751–2762. <https://doi.org/10.1002/2016JB013767>
- Hu H, Dai L, Li H, Sun W, Li B (2018) Effect of dehydrogenation on the electrical conductivity of Fe-bearing amphibole: Implications for high conductivity anomalies in subduction zones and continental crust. *Earth Planet Sci Let* 498:27–37. <https://doi.org/10.1016/j.epsl.2018.06.003>
- Ichiki M, Ogawa Y et al (2015) Electrical image of subduction zone beneath northeastern Japan. *J Geophys Res Solid Earth* 120:7937–7965. <https://doi.org/10.1002/2015JB012028>
- Karato S-i, Wang D (2013) Electrical conductivity of minerals and rocks. In: Karato S-i (ed) *Physics and chemistry of the deep earth*. Wiley Blackwell, NY, pp 145–182
- Kasaya T, Tn G, Mikada H, Baba K, Suyehiro K, Utada H (2005) Resistivity image of the Philippine Sea Plate around the 1944 Tonankai earthquake zone deduced by Marine and Land 579 MT surveys. *Earth Planet Space* 57:209–213. <https://doi.org/10.1186/BF03351817>
- Katsura T, Yoshino T, Manthilake G, Matsuzaki T (2009) Electrical conductivity of the major upper mantle minerals: a review. *Russian Geol Geophys* 50:1139–1145
- Kimura J-I, Nakajima J (2014) Behaviour of subducted water and its role in magma genesis in the NE Japan arc: A combined geophysical and geochemical approach. *Geochim Cosmochim Acta* 143:165–188
- Li Y, Yang X, Yu J-H, Cai Y-F (2016) Unusually high electrical conductivity of phlogopite: the possible role of fluorine and geophysical implications. *Contrib Mineral Petrol* 171:37. <https://doi.org/10.1007/s00410-016-1252-x>
- Littler JGF, Williams RJP (1965) Electrical and optical properties of crocidolite and some other iron compounds. *J Chem Soc* 1182:6368–6371. <https://doi.org/10.1039/JR9650006368>
- Manthilake G, Bolfan-Casanova N, Novella D, Mookherjee M, Andraut D (2016) Dehydration of chlorite explains anomalously high electrical conductivity in the mantle wedges. *Sci Adv*. <https://doi.org/10.1126/sciadv.1501631>
- Merlin R, Pinczuk A, Weber WH (2000) Overview of phonon raman scattering in solids. In: Weber WH, Merlin R (eds) *Raman scattering in materials science*, springer series in materials science 42. Springer, pp 1–29
- Mihailova B, Della Ventura G, Waesermann N, Xu W, Schlüter J, Galdenzi F, Marcelli A, Redhammer GJ, Boiocchi M, Oberti R (2021) Atomistic insight into lithospheric conductivity revealed by phonon-electron excitations in hydrous iron-bearing silicates. *Comm Mat* 2:1–10. <https://doi.org/10.1038/s43246-021-00161-y>
- Mihailova B, Della Ventura G, Waesermann N, Bernardini S, Xu W, Marcelli A (2022) Polarons in rock-forming minerals: physical implications, *Cond. Matter* 7:68. <https://www.mdpi.com/2410-3896/7/4/68>
- Momma K, Izumi F (2008) VESTA: a three-dimensional visualization system for electronic and structural analysis. *J Appl Cryst* 41:653–658
- Oberti R, Della Ventura G, Cámara F (2007) New amphibole compositions: natural and synthetic. *New Amphibole Composit: Nat Synthetic*. 67:89–124
- Oberti R, Boiocchi M, Zema M, Della Ventura G (2016) Synthetic potassic-ferro-richterite: 1. Composition, crystal structure refinement and HT behavior by in operando single-crystal X-ray diffraction. *Can Mineral* 54:353–369
- Oberti R, Boicchi M, Zema M, Hawthorne FC, Redhammer GJ, Susta U, Della Ventura G (2018) The high-temperature behaviour of riebeckite: expansivity, deprotonation, selective Fe oxidation and a novel cation disorder scheme for amphiboles. *Eur J Mineral* 30:437–449
- Parkomenko EI (1982) Electrical resistivity of minerals and rocks at high temperature and pressure. *Rev Geophys Space Phys* 20:193–218. <https://doi.org/10.1029/RG020i002p00193>
- Peacock SM, Wang K (1996) Seismic consequences of warm versus cool subduction metamorphism: examples from Southwest and Northeast Japan. *Science* 286:937–939
- Phillips MW, Popp RK, Clowe CA (1988) Structural adjustments accompanying oxidation-dehydrogenation in amphiboles. *Am Mineral* 73:500–506
- Phillips MW, Draheim JE, Popp RK, Clowe CA, Pinkerton AA (1989) Effect of oxidation-dehydrogenation in tschermakitic hornblende. *Am Mineral* 74:764–773
- Phillips MW, Popp RK, Clowe CA (1991) A structural investigation of oxidation effects in air-heated grunerite. *Am Mineral* 76:1502–1509
- Pommier A (2014) Geophysical assessment of migration and storage conditions of fluids in subduction zones. *Earth Planets Space* 66:1–11. <https://doi.org/10.1186/1880-5981-66-38>
- Redhammer GJ, Beran A, Schneider J, Amthauer G, Lottermoser W (2000) Spectroscopic and structural properties of synthetic micas on the annite- siderophyllite binary: synthesis, crystal structure refinement, Mössbauer, and infrared spectroscopy. *Am Mineral* 85:449–465
- Robert J-L, Beny J-M, Beny C, Volfinger M (1989) Characterization of lepidolites by Raman and infrared spectrometries. I. Relationships between OH-stretching wavenumbers and composition. *Can Mineral* 27:225–235
- Rösche C, Waesermann N, Petrova N, Malcherek T, Schlüter J, Mihailova B (2022) Oxidation processes and thermal stability of actinolite. *Phys Chem Mineral* 49:1–17. <https://doi.org/10.1007/s00269-022-01223-4>
- Schmidbauer E, Kunzmann T, Fehr T, Hochleitner R (1996) Electrical conductivity, thermopower and ⁵⁷Fe Mössbauer spectroscopy on an Fe-rich amphibole, arfvedsonite. *Phys Chemistry Mineral* 23:99–106
- Schmidbauer E, Kunzmann T, Fehr T, Hochleitner R (2000) Electrical resistivity and ⁵⁷Fe Mössbauer spectra of Fe-bearing calcic amphiboles. *Phys Chem Mineral* 27:347–356. <https://doi.org/10.1007/s002690050264>
- Shen K, Wang D, Liu T (2020) Electrical conductivity of tremolite under high temperature and pressure: implications for the high-conductivity anomalies in the Earth and Venus. *Contrib Mineral Petrol* 175:52. <https://doi.org/10.1007/s00410-020-01688-y>
- Syracuse EM, van Keken PE, Abers GA (2010) The global range of subduction zone thermal models. *Phys Earth Planet Inter* 183:73–90. <https://doi.org/10.1016/j.pepi.2010.02.004>
- Tolland HG (1973) Mantle conductivity and electrical properties of garnet, mica and amphibole. *Nature* 241:35–36
- Turci F, Tomatis M, Pacella A (2017) Surface and bulk properties of mineral fibres relevant to toxicity. In: Gualtieri AF (ed) *Mineral fibres: crystal chemistry, chemical physical properties, biological*

- interaction and toxicity, 18, EMU Notes in Mineralogy, pp 171–214
- Ungaretti L (1980) Recent developments in X-ray single crystal diffractometry applied to the crystal-chemical study of amphiboles. *Godisnjak Jugoslavenskog Centra Za Kristalografiju* 15:29–65
- Vigliaturo R, Jamnik M, Dražić G, Podobnik M, TušekŽnidarič M, Della Ventura G, Redhammer G, Nada Z, Caserman S, Gieré R (2022) Nano-scale transformations of amphiboles within human alveolar epithelial cells. *Sci Rep* 12:1782. <https://doi.org/10.1028/s41598-022-05802-x>
- Wang D, Karato S-i (2013) Electrical conductivity of talc aggregates at 0.5 GPa: influence of dehydration. *Phys Chem Miner* 40:11–17. <https://doi.org/10.1007/s00269-012-0541-9>
- Wang D-J, Li H-P, Liu C-Q et al (2002) Electrical conductivity of synthetic quartz crystals at high temperature and pressure from complex impedance measurements. *Chin Phys Lett* 19:1211–1213
- Wang D, Guo Y, Yu Y, Karato S-i (2012) Electrical conductivity of amphibole-bearing rocks: influence of dehydration. *Contrib Mineral Petrol* 164:17–25
- Withfield HJ, Freeman AG (1967) Mössbauer study of amphiboles. *J Inorg Nucl Chem* 29:903–914
- Yang X, Keppler H, McCammon C, Ni H (2012) Electrical conductivity of orthopyroxene and plagioclase in the lower crust. *Contrib Mineral Petrol* 163:33–48
- Yoshino T, Katsura T (2013) Electrical conductivity of mantle minerals: role of water in conductivity anomalies. *Annu Rev Earth Planet Sci* 41:605–628. <https://doi.org/10.1146/annurev-earth-050212-124022>
- Yoshino T, Matsuzaki T, Yamashita S, Katsura T (2006) Hydrous olivine unable to account for conductivity anomaly at the top of the asthenosphere. *Nature* 443:973–976. <https://doi.org/10.1038/nature05223>
- Yu P, Cardona M (2010) *Fundamentals of Semiconductors*. Springer
- Zang M, Wang L, Hirai S, Redfern SA, Salje EKH (2005) Dehydration and CO₂ incorporation in annealed mica (sericite): an infrared spectroscopic study. *Am Mineral* 90:173–180
- Zang M, Hui Q, Lou XJ, Redfern SA, Salje EKH, Tarantino SC (2006) Dehydration, proton migration, and structural changes in heated talc: an infrared spectroscopic study. *Am Mineral* 91:816–825

Publisher's Note Springer Nature remains neutral with regard to jurisdictional claims in published maps and institutional affiliations.

Springer Nature or its licensor (e.g. a society or other partner) holds exclusive rights to this article under a publishing agreement with the author(s) or other rightsholder(s); author self-archiving of the accepted manuscript version of this article is solely governed by the terms of such publishing agreement and applicable law.